Correspondence to:

N. V. Solomatova and R. Caracas,
natalia.solomatova@ens-lyon.fr; razvan.caracas@ens-lyon.fr

Buoyancy and Structure of Volatile-Rich Silicate Melts

Natalia V. Solomatova[1] and **Razvan Caracas[1,2]**

[1]CNRS, Ecole Normale Supérieure de Lyon, Laboratoire de Géologie de Lyon LGLTPE UMR5276, Centre Blaise Pascal, Lyon, France, [2]The Center for Earth Evolution and Dynamics (CEED), University of Oslo, Oslo, Norway

Abstract The early Earth was marked by at least one global magma ocean. Melt buoyancy played a major role for its evolution. Here we model the composition of the magma ocean using a six-component pyrolite melt, to which we add volatiles in the form of carbon as molecular CO or CO_2 and hydrogen as molecular H_2O or through substitution for magnesium. We compute the density relations from first-principles molecular dynamics simulations. We find that the addition of volatiles renders all the melts more buoyant compared to the reference volatile-free pyrolite. The effect is pressure dependent, largest at the surface, decreasing to about 20 GPa, and remaining roughly constant to 135 GPa. The increased buoyancy would have enhanced convection and turbulence, and thus promoted the chemical exchanges of the magma ocean with the early atmosphere. We determine the partial molar volume of both H_2O and CO_2 throughout the magma ocean conditions. We find a pronounced dependence with temperature at low pressures, whereas at megabar pressures the partial molar volumes are independent of temperature. At all pressures, the polymerization of the silicate melt is strongly affected by the amount of oxygen added to the system while being only weakly affected by the specific type of volatile added.

1. Introduction

It is particularly challenging to experimentally measure the density of silicate melts at the pressures and temperatures of Earth's deep mantle (Sanloup, 2016; Sanloup et al., 2013; Thomas et al., 2012; Xu et al., 2020). *In situ* measurements using shock compression (e.g., Rigden et al., 1984), the sink-float method in a multianvil press (e.g., Agee & Walker, 1988) and X-ray absorption spectroscopy (e.g., Sakamaki et al., 2010) have mostly been limited to uppermost-mantle conditions. The bulk of experimental studies on the compressibility of amorphous silicate systems at the conditions of the lower mantle have been conducted on silicate glasses as proxies for silicate melts (Kono et al., 2018; Murakami & Bass, 2010; Park & Lee, 2018; Petitgirard, 2017; Prescher et al., 2017; Wu et al., 2012). Pressure-density-temperature relations of complex silicate melts can be calculated from first-principles molecular dynamics simulations, offering an excellent alternative to *in situ* experiments (Bajgain et al., 2015; Caracas et al., 2019; de Koker et al., 2013; Karki et al., 2018; Sahle et al., 2013; Spiekermann et al., 2016; Stixrude et al., 2009).

Buoyancy relations of magmas are the major driving force for melt transport inside the Earth. In the early Earth, dominated by the magma ocean stage, the high temperatures combined with the correspondingly low viscosity of the molten silicates would have made extreme turbulence prevalent in the first stages of convection. As the Earth lost heat, the temperature would have started to drop, making the density differences more important for the general circulation in the global magma ocean. Regardless of the crystallization path, it is highly foreseeable that a mushy layer of interconnected crystals and interstitial molten silicate may stabilize in the middle of the magma ocean (Caracas et al., 2019; Labrosse et al., 2007). If this mushy layer was continuous, an insulated basal magma ocean could have persisted up to 1–2 billion years (Ballmer, Lourenço, et al., 2017; Trønnes et al., 2019). If the mushy layer were not continuous, wide patches of primitive crystals may have survived convection and mixing into the mantle up to present day in the form of bridgmanite-enriched ancient mantle structures (Ballmer, Houser, et al., 2017); the magma flow would have taken place around these structures. Nevertheless, as the crystallization advanced, the density of the liquids and their relation to the density of the solids played an even more important role (Trønnes et al., 2019).

Fractional crystallization of the magma ocean would have extracted the iron-poor $MgSiO_3$ component from the melt, which crystallized as bridgmanite (Ballmer, Lourenço, et al., 2017). As the crystallization

advanced, the crystals contained an increasingly large amount of iron; however, the melt would have still been relatively enriched in heavy components, such as FeO and CaO, due to chemical partitioning (Andrault et al., 2012; Fiquet et al., 2010; Nomura et al., 2011). Today, geodynamic models of the crystallization of the magma ocean take into account the relative evolution of the density with changing chemistry for both silicate magma and crystals (Ballmer, Lourenço, et al., 2017).

Current models tend to ignore the presence of a volatile component in the magma ocean due to an acute lack of data. However, a certain amount of volatiles must have been present from the beginning of accretion, brought to the proto-Earth by chondritic material. Indeed, ordinary chondrites typically contain up to a few percent of complex carbon- and hydrogen-based organic matter (Cody et al., 2011). Although some of the volatiles likely escaped during the Giant Impact event, a fair amount must have been trapped in the protolunar disk (Canup, 2012) or the synestia (Ćuk & Stewart, 2012; Lock et al., 2018). An additional amount may have been sequestered from the magma ocean into the core during core formation (Solomatova et al., 2019), and another fraction likely degassed to form the early atmosphere (Elkins-Tanton, 2008). The remaining amount was dissolved into the molten magma ocean, and as such would have participated in convection, influencing the density of the hosting magmas. Any advent of volatile-bearing material through late impacts would have created pockets of volatile-rich silicate melts, which would have behaved differently from the surrounding magma ocean, in terms of density and viscosity.

In order to address the effect of volatiles on the density and structure of silicate melts, we use *ab initio* molecular dynamics simulations to calculate the equations of state (EOS) and degrees of polymerization of pyrolite melts with varying concentrations of volatiles. The effect of volatiles on the relative buoyancy of each melt is quantified and the implications for the general circulation of the global magma ocean are discussed.

2. Methodology

We employ first-principles molecular dynamics simulations to study the pressure and temperature dependence of a series of realistic silicate melts whose compositions approximate the global magma ocean. In molecular dynamics, the particles (i.e., the atoms) move under the action of interatomic forces according to Newtonian mechanics. With first principles we accurately compute these interatomic forces without relying on any approximations and fits to experimental data. We use the density functional theory in the planar-augmented wavefunction flavor as implemented in the VASP package (Kresse & Furthmüller, 1996; Kresse & Hafner, 1993) to compute the interatomic forces. The kinetic energy cutoff of the planewaves was set at 550 eV and the augmentation charge at 800 eV. The electronic density is sampled in the reciprocal space in the Gamma point. With these parameters, the accuracy of the pressure is on the order of a few kilobars. We employ the generalized gradient approximation (GGA) in the Perdew-Burke-Ernzerhof formulation (Perdew et al., 1996) for the exchange-correlation term. Because of the presence of iron, all the simulations are spin-polarized, with the spin on each Fe atom being allowed to freely fluctuate at each time step. All simulations were performed in the NVT ensemble, where the number of particles (N), the volume (V), and the temperature (T) of the system are kept constant throughout the simulations. The temperature is fixed using a Nosé-Hoover thermostat. The time step for the pure and carbonated melts was 1 fs, which is short enough to capture the vibrational modes present in the melt. For the hydrous melts, the timestep was reduced to 0.5 fs that allowed properly capturing the vibrations in which the light hydrogen atoms participate. Simulations were conducted at temperatures of 2000, 3000, 4000, and 5000 K. In typical NVT simulations, both pressure and temperature fluctuate around average values; their excursions describe a normal distribution. For example, at 4000 K, we obtain a standard deviation in pressure of 1.5 GPa at ambient pressure, increasing to 3 GPa at 150 GPa; the median (i.e., the range between 25% and 75% of the values) is on the order of 2 GPa at ambient pressure, increasing to 3.5 GPa at high pressure. These values show a small deviation of the pressure from the average, with limited and symmetric excursions above and below it. The fluctuations of both temperature and pressure can be reduced by increasing the size of the supercell; however, increasing the number of atoms makes the simulations untractable. The size of our simulations is in the typical range for *ab initio* molecular dynamics studies (Bajgain et al., 2015; de Koker et al., 2013; Sahle et al., 2013; Spiekermann et al., 2016; Stixrude et al., 2009). The standard deviation on the pressure fluctuations are used to represent the uncertainty in pressure. We find that the errors from block-based analysis underestimate the true uncertainty in pressure and do not capture the error associated with the

Table 1
Volatile Concentrations in Pyrolite Melt Reported as Elemental Weight Percent, Elemental Mole Percent and Oxide Weight percent

	wt% H	mol.% H	wt% H_2O	wt% C	mol.% C	wt% CO_2	No. atoms
pure pyrolite ("py")	0	0	0	0	0	0	155
py-2Mg+4H	0.13	2.58	1.13	0	0	0	157
py-4Mg+8H	0.26	5.10	2.29	0	0	0	161
py-8Mg+16H	0.53	9.94	4.72	0	0	0	165
py+4H_2O	0.24	4.85	2.18	0	0	0	177
py+8H_2O	0.48	9.04	4.27	0	0	0	161
py+4CO	0	0	0	1.44	2.48	5.26	165
py+4CO_2	0	0	0	1.41	2.42	5.16	169
py+8CO	0	0	0	2.78	4.73	10.2	177
py+8CO_2	0	0	0	2.68	4.52	9.82	166
py-2Mg-Si+8H+4CO	0.25	4.82	2.20	1.47	2.41	5.37	155

Note. The last column indicates the total number of atoms within the supercell. Periodic boundary conditions are implemented.

spread in pressures based on the choice of different starting configurations, the length of the simulations and the cutoff length for thermalization, which is typical in first-principles molecular dynamics simulations of fluids. The cumulative effect of these errors results in a pressure uncertainty of roughly 3%, which is well represented by the standard deviation on the pressure fluctuations of the simulations.

The reference melt has the pyrolite composition, which is an approximant to the bulk silicate Earth composition (McDonough & Sun, 1995), and which already served in previous studies (Caracas et al., 2019; Solomatova & Caracas, 2019; Solomatova et al., 2019). It is a six-component melt with a molar composition of $0.5Na_2O-2CaO-1.5Al_2O_3-4FeO-30MgO-24SiO_2$. This composition is within 1 wt% to the proposed bulk silicate Earth composition. We use cubic cells with 153 atoms to mimic the dry pyrolitic composition. The initial melts are obtained starting with the garnet conventional cell where the atoms are arranged as best as possible to their standard coordination by oxygen in solid silicate minerals. The garnet cells are heated up to 5000 K in 1 K/fs steps and kept at 5000 K for at least 1 ps. By this time the silicate is molten, as observed in the finite mean square displacement of all the atoms. Then the melt is cooled down to the needed temperature in steps of 1 K/fs and it is kept for at least 1 ps at the final temperature before any statistics start to be recorded. This thermalization period ensures that the kinetic energy of all the atoms reach a normal Gaussian distribution around the target temperature. The length of the simulations is between 10 and 20 ps after a thermalization period of about 1 ps. Long atomic trajectories give atoms enough time to exchange their site at least once and to sample several local configurations. This criterion is important to ensure that we reach ergodicity (i.e., sampling a relevant part of the configurational space; Harvey & Asimow, 2015).

Carbon is added to the reference 153-atom pyrolite melt in the form of four CO units ("py+4CO"), eight CO units ("py+8CO"), four CO_2 units ("py+4CO_2") and eight CO_2 units ("py+8CO_2"), resulting in melts with 1.4–2.8 wt% C (Table 1). Molecular water is added to the pyrolite melt in two concentrations ("py+4H_2O" and "py+8H_2O"), resulting in melts with 0.24 wt% and 0.48 wt% H, respectively. Hydrogen is also added through the Mg ⇔ 2H substitution, in three concentrations ("py-2Mg+4H," "py-4Mg+8H", and "py-8Mg+16H"), resulting in melts with 0.13–0.53 wt% H. In order to minimize the effect of hydrogen substitution on the Mg:Si ratio, we also consider one substitution to incorporate atomic hydrogen as 2 Mg + Si ⇔ 8H. We couple the latter substitution with the addition of four CO molecules to have a simulation of a melt that is both carbonated and hydrous ("py-2Mg-Si+8H+4CO"). The molecular groups, CO, CO_2, and H_2O, are added in the interstitial voids of pyrolite melt at low pressure. Subsequently, the melts are thermalized, and the stresses induced by the presence of the extra molecules are released and accommodated by the melt. The melts are then compressed in about 6–10 steps along several isotherms (3000 K, 4000 K, and 5000 K) to cover the entire pressure and temperature range of the magma ocean. Table 1 lists the compositions of all the melts
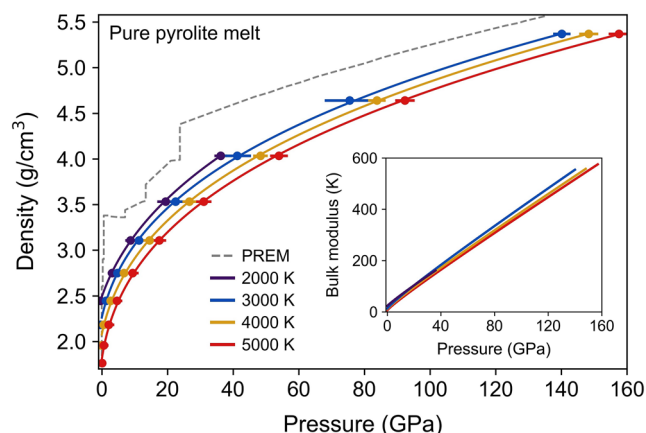
Figure 1. Third-order Birch Murnaghan equations of state fitted to the pressure-density data for pure volatile-free pyrolite from *ab initio* molecular dynamics simulations at 2000 K (purple), 3000 K (blue), 4000 K (yellow), and 5000 K (red). PREM is shown as a dashed gray line for reference. Inset shows the bulk modulus as a function of pressure.

in this study. For comparison with experimental data, we also compress pure pyrolite melt, pyrolite melt with $4CO_2$ (5.16 wt% CO_2) and pyrolite melt with $4H_2O$ (2.18 wt% H_2O) to mid-mantle pressures at 2000 K.

Doubling the number of atoms within the periodically repeated supercell does not change the thermodynamic or structural properties. We compared the results of our simulations on pyrolite + 5.16 wt% CO_2 with 161 and 322 atoms. For the 322-atom supercell, we performed non-spin-polarized calculations due to the expensive computational costs; the effect of spin-polarization on density has been shown to be within 1% for MORB and bridgmanite melts (Bajgain et al., 2015; Caracas et al., 2019; Karki et al., 2018). The calculated pressures were –0.1(7) GPa and −0.1(5) GPa while the internal energies per atom were −5.71(5) eV and −5.70(4) eV for the cells with 161 atoms and 322 atoms, respectively, where values in parentheses denote standard deviations. Thus, both pressure and energy were found to be within error and nearly identical. Likewise, the local coordination of the cations by oxygen was found to be within 2% despite the fact that the 322-atom cell was non-spin polarized.

3. Results and Discussion

Using *ab initio* molecular dynamics simulations, we determine the pressure-density relations of volatile-free and volatile-bearing pyrolite melts with 0.13–0.48 wt% H (1.13–4.72 wt% H_2O) and 1.41–2.78 wt% C (5.16–10.2 wt% CO_2) along isotherms of 3000 K, 4000 K, and 5000 K over a pressure range of 0–150 GPa. To directly compare to experimental data, we also perform simulations at 2000 K on volatile-free and volatile-bearing pyrolite melts with 4.85 wt% H and 2.42 wt% C over a pressure range of about 0–40 GPa. Section 3.1 describes the results of fitting third-order Birch-Murnagham (BM) EOS to the pressure-density data with implications for buoyancy and convection of the global magma ocean. In Section 3.2, we discuss the partial molar volumes of H_2O and CO_2 as a function of pressure and temperature with direct comparisons to previous experiments and simulations. Finally, the structural effects of adding volatiles to pyrolite melt are discussed in Section 3.3.

3.1. Equations of State

A third-order Birch-Murnaghan (BM) EOS was fitted to the pressure-density data from the *ab initio* molecular dynamics simulations. A fourth-order EOS was not warranted, as shown through an analysis of the normalized pressure (F) plotted against Eulerian strain (f) (see Figure S1). In any case, the choice of using a third-order or fourth-order Birch-Murnaghan EOS has only a negligible effect on the relative densities (Figure S2). Between 0 and about 40 GPa, pyrolite melt undergoes rapid densification as the coordination numbers of the cations by oxygen atoms sharply increase (Solomatova & Caracas, 2019), meaning that the density increases more rapidly at upper-mantle pressures and more gradually with increasing pressure. Pure pyrolite melt is less dense than the solid mantle, modeled with the preliminary reference Earth model (Dziewonski & Anderson, 1981), by about 0.5–1.0 g/cm^3, depending on the temperature of the melt (Figure 1). There is a density crossover between pyrolite melt and the crystallizing bridgmanite in the lower part of the magma ocean, gradually moving toward mid-depths with increasing crystallization rate (Caracas et al., 2019).

The fitted third-order EOS parameters (e.g., density at ambient pressure, ρ_0, bulk modulus, K, and the first derivative of the bulk modulus, K′) are listed in Table 2. At 2000 K, the computed zero-pressure bulk modulus (K_0) is 24 (2) GPa and a first-order pressure derivative (K_0') of 4.7 (2) in general agreement with literature values of K_0 = 24–32 GPa and K_0' = 4–6 at 2100–2300 K (Figure S3; Agee, 1998; Agee & Walker, 1993; Sakamaki et al., 2009; Suzuki & Ohtani, 2003). Our zero-pressure density is underestimated at 2.49 (2) g/cm^3 relative to the experimental value of ~2.7 g/cm^3 possibly due to the use of the GGA exchange-correlation functional, which tends to underestimate the cohesive energies and thus overestimates bond lengths; how-

Table 2
Zero-Pressure Density (ρ_0), Zero-Pressure Bulk Modulus (K_0), First Derivative of the Bulk Modulus (K'), Density at 135 GPa (ρ_{135}) and Bulk Modulus at 135 GPa (K_{135}) at 2000–5000 K, Obtained From Fitting a Third-Order Birch Murnaghan (BM) Equation of State to the Pressure-density Data From the ab initio Molecular Dynamics Simulations

T = 2000 K	ρ_0 (g/cm^3)	K_0 (GPa)	K'	ρ_{135} (g/cm^3)	K_{135} (GPa)
pure pyrolite ("py")	2.49 (2)	24 (2)	4.7 (2)	–	–
py+4H$_2$O	2.32 (3)	15 (2)	5.5 (3)	–	–
py+4CO$_2$	2.37 (5)	18 (3)	5.0 (4)	–	–
T = 3000 K	ρ_0 (g/cm^3)	K_0 (GPa)	K'	ρ_{135} (g/cm^3)	K_{135} (GPa)
pure pyrolite ("py")	2.26 (2)	14 (1)	5.7 (2)	5.32 (1)	536 (4)
py-2Mg+4H	2.17 (3)	11 (2)	6.1 (3)	5.32 (2)	544 (10)
py-4Mg+8H	2.13 (4)	11 (1)	6.0 (3)	5.26 (1)	534 (5)
py-8Mg+16H	1.98 (5)	8 (1)	6.4 (4)	5.20 (1)	533 (3)
py+4H$_2$O	2.11 (6)	10 (2)	6.3 (4)	5.24 (1)	540 (4)
py+4CO	2.11 (7)	9 (2)	6.5 (5)	5.29 (2)	541 (7)
py+4CO$_2$	2.12 (7)	10 (2)	6.2 (4)	5.27 (1)	538 (5)
T = 4000 K	ρ_0 (g/cm^3)	K_0 (GPa)	K'	ρ_{135} (g/cm^3)	K_{135} (GPa)
pure pyrolite ("py")	2.08 (3)	12 (1)	5.4 (1)	5.24 (1)	512 (2)
py-2Mg+4H	2.01 (2)	10.6 (8)	5.4 (1)	5.21 (1)	510 (2)
py-4Mg+8H	1.94 (2)	8.9 (6)	5.6 (1)	5.18 (1)	512 (2)
py-8Mg+16H	1.74 (4)	5.2 (8)	6.2 (2)	5.11 (1)	512 (2)
py+4H$_2$O	1.94 (6)	9 (1)	5.6 (2)	5.16 (1)	513 (3)
py+8H$_2$O	1.81 (6)	7 (1)	5.6 (2)	5.09 (1)	505.7 (5)
py+4CO	1.85 (5)	6 (1)	6.2 (3)	5.20 (1)	517 (4)
py+4CO$_2$	1.92 (3)	8.2 (9)	5.8 (2)	5.18 (1)	515 (2)
py+8CO	1.69 (6)	4 (1)	6.7 (5)	5.16 (1)	515 (2)
py+8CO$_2$	1.86 (4)	7 (1)	5.8 (3)	5.15 (1)	512 (3)
py-2Mg-Si+8H+4CO	1.78 (3)	6.1 (6)	5.9 (1)	5.13 (1)	509 (1)
T = 5000 K	ρ_0 (g/cm^3)	K_0 (GPa)	K'	ρ_{135} (g/cm^3)	K_{135} (GPa)
pure pyrolite ("py")	1.80 (4)	7.2 (9)	5.5 (2)	5.15 (2)	499 (3)
py-2Mg+4H	1.73 (6)	6 (1)	5.6 (2)	5.11 (1)	497 (3)
py-4Mg+8H	1.53 (7)	3 (1)	6.0 (4)	5.08 (4)	495 (5)
py-8Mg+16H	1.47 (7)	2.8 (9)	6.4 (5)	5.00 (2)	498 (3)
py+4H$_2$O	1.66 (7)	6 (1)	5.6 (3)	5.06 (2)	498.8 (4)
py+4CO	1.60 (5)	4.1 (8)	6.0 (3)	5.11 (1)	498 (3)
py+4CO$_2$	1.65 (7)	5 (1)	5.8 (3)	5.10 (2)	497 (3)

ever, the relative densities between the various melts should not be affected by the choice of exchange-correlation functional.

As a general rule, we predict that the bulk moduli of the dry non-carbonated pyrolite melt are higher compared to the bulk moduli of the volatile-bearing melts. The melts where carbon is present as CO$_2$ have higher compressibilities than the ones in which carbon is present as CO. We do not observe any consistent differences between atomic hydrogen and molecular water along the 4000 K isotherm, where we tested both forms; the same is valid between different amounts of hydrogen. Experiments on peridotite melt at approximately 2000 K predict that K_0 decreases by 60% upon adding 4.8 wt% H$_2$O while it was unaffected
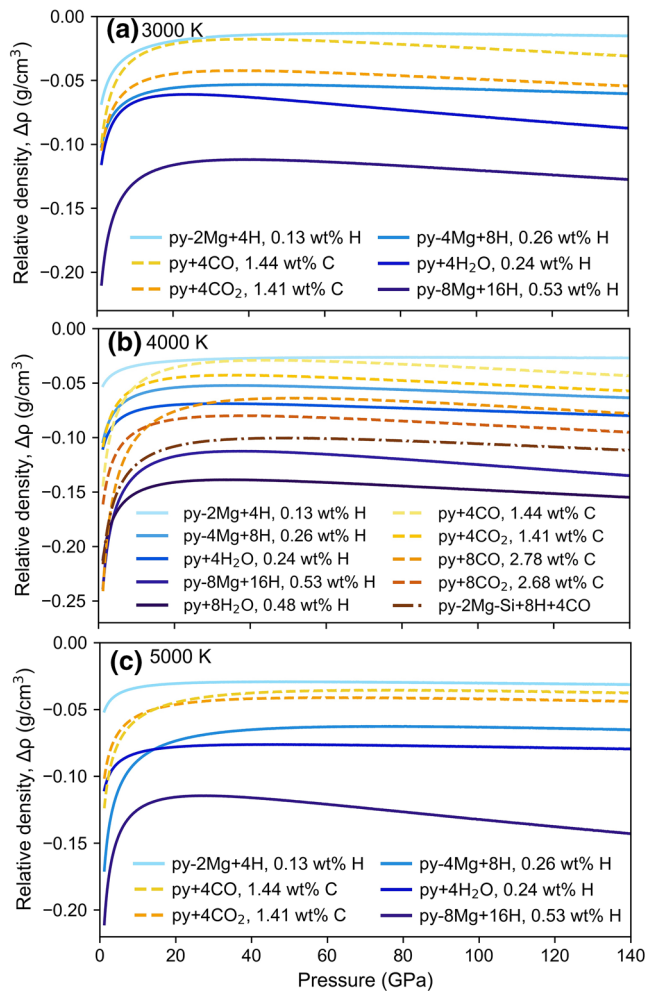
Figure 2. Difference in density between volatile-bearing pyrolite melts with respect to volatile-free pure pyrolite melt at (a) 3000 K, (b) 4000 K and (c) 5000 K, as obtained from third-order Birch-Murnagham equations of state. The addition of volatiles renders the melts more buoyant relative to volatile-free pyrolite melt. The buoyancy of volatile-bearing pyrolite melts generally increases with increasing volatile content and the addition of hydrogen-bearing volatiles generally has a stronger effect compared to the addition of carbon-bearing volatiles.

by the addition of 2.5 wt% CO_2 (Sakamaki et al., 2011). In our simulations, at 3000–5000 K, the addition of either CO_2 or H_2O decreases K_0 by 10–60%, generally increasing with increasing volatile concentration; for example, the addition of 2.2 wt% H_2O or 5.2 wt% CO_2 both decrease K_0 about 30% at 3000 K. In contrast, at 135 GPa the effect of volatiles on the bulk modulus is negligible (within 1.5% and mostly within error). At high pressures, the addition of volatile species does not make the melt much more compressible, as it has reached, in some sense, a compressibility limit, whereas at low pressure, before the melt undergoes rapid densification, the addition of volatiles in the form of H_2O or CO_2, or by replacing cations, such as magnesium by hydrogen, results in a more compressible melt.

Recent *ab initio* molecular dynamics simulations on enstatite melt at 3000 K predict zero-pressure bulk moduli of 19.1(1.6), 6.7(7) and 8.2(8) GPa for pure enstatite ($32MgSiO_3$), enstatite with 2.7 wt% C ($32MgSiO_3 + 8CO_2$) and enstatite with 0.91 wt% H ($32MgSiO_3 + 16H_2O$), respectively (Karki et al., 2020), indicating that the bulk modulus decreases with the addition of volatiles. The drop in bulk modulus due to the addition of volatiles appears to be greater in $MgSiO_3$ compared to in pyrolite, likely due to the simpler chemistry, and thus a more significant disruption of the silica network, resulting in easier compressibility.

The addition of volatiles, both carbon and hydrogen, to pure pyrolite reduces the density of the melt at ambient pressure conditions (i.e., ρ_0). The effect is roughly proportional to the amount of volatiles incorporated in the melt. At high pressures, the relative density relations become more interesting. Figure 2 shows the difference in density between the volatile-bearing and pure pyrolite at three temperatures: 3000 K, 4000 K, and 5000 K. Negative values correspond to relatively more buoyant melts. All the volatile-bearing melts are buoyant with respect to the dry volatile-free pyrolite, at all temperatures and pressures examined in this study. The density difference is more pronounced in the first part of the compression, up to about 20 GPa. Then with increasing pressure the difference either plateaus or slightly increases. For the carbonated melts at 3000 K and 4000 K there is a clear dependence of the density depression with the amount of carbon, and with the type of carbon volatile added, the CO_2-bearing melts being more buoyant than the CO-bearing ones, whereas at 5000 K the difference is leveled off.

The same proportionality is valid between buoyancy and the amount of hydrogen. The melts with the largest amount of hydrogen in the simulations show the largest buoyancy. There is only a small difference in the degree of buoyancy between the melts with molecular water and those with atomic hydrogen. Indeed, as the water molecules dissociate in the melt, the amount of hydroxylation of the melt appears to be the strongest factor governing buoyancy. Although, the relative densities of the melts are only weakly affected by the mechanism by which we added hydrogen, the polymerization of the melts is strongly dependent on the form in which we add the volatiles (see Section 3.3).

3.2. Partial Molar Volumes

We calculated the partial molar volumes as a function of pressure and temperature by subtracting the EOS of hydrated and carbonated pyrolite melts from the EOS of dry pyrolite. Our calculated partial molar volumes at 2000 K are generally in good agreement with experiments (Figures 3 and 4). Experimental data in Figure 3 correspond to the reported values in the respective studies, except for the partial molar volume
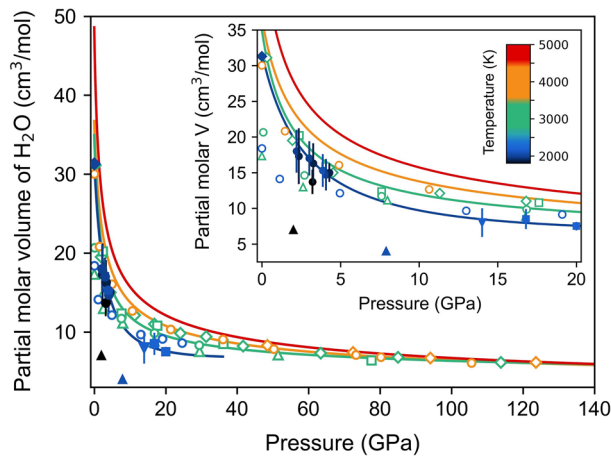
Figure 3. Partial molar volumes of H_2O in magmatic melts. Curves are the results of our simulations of pyrolite + $4H_2O$ (2.2 wt% H_2O) at 2000 K (blue), 3000 K (green), 4000 K (orange) and 5000 K (red). Experimental data are shown as filled symbols: albite melt with 1.9–6.1 wt% H_2O at 2000 K (diamond; Ochs & Lange, 1997), pyrolite melt with 5 wt% H_2O at 2170 K (downward-pointing triangles; Matsukage et al., 2005), basalt melt with 8 wt% H_2O at 2200 K (squares; Sakamaki et al., 2006), komatiite-fayalite mixture with 2–5 wt% H_2O at 1773 and 2073 K (upward-pointing triangles; Agee, 2008), and peridotite melt with 5 wt% H_2O at 1773–2073 K (circles; Sakamaki et al., 2009). Data from *ab initio* molecular dynamics simulations are shown as open symbols: silica melt with 8.25 wt% H_2O at 3000 K (open triangles; Bajgain et al., 2015; Karki & Stixrude, 2010), enstatite melt with 4.5 wt% H_2O at 3000–4000 K (open diamonds; Karki et al., 2020), enstatite melt with 10 wt% H_2O at 3000 K (open squares; Mookherjee et al., 2008), and basalt melt with 5 wt% H_2O at 2200–4000 K (Bajgain et al., 2015). Inset shows a magnification of the 0–20 GPa region.

of H_2O in albite at 1 bar (Ochs & Lange, 1997) where we use their reported temperature dependence of the partial molar volume of H_2O to extrapolate to 2000 K, as no other data is available at ambient pressure and ~2000 K. At ambient pressure and 2000 K, we calculate a partial molar volume of 31.7 cm^3/mol, similar to the experimental value of 31.3(6) cm^3/mol in albite melt (Ochs & Lange, 1997), despite the different melt compositions.

The calculated compressibility behavior of H_2O in our pyrolite melt agrees very well with experiments and *ab initio* simulations on ultramafic compositions, including peridotite melt with 5 wt% H_2O at 1773–2200 K (Sakamaki et al., 2009), pyrolite melt with 5 wt% H_2O at 2170 K (Matsukage et al., 2005) and enstatite melt with 4.5 wt% H_2O at 3000–4000 K (Karki et al., 2020; Mookherjee et al., 2008) (Figure 3). However, the partial molar volumes of H_2O are lower in the more polymerized melts (i.e., basalt melt with 5 wt% H_2O at 2200–4000 K and silica melt with 8.25 wt% H_2O at 3000 K) at pressures of 0–10 GPa (Bajgain et al., 2015; Karki & Stixrude, 2010). At higher pressures, there is no observable sensitivity of the partial molar volume of H_2O to the composition of the melt; instead, there is very good agreement between the partial molar volumes of H_2O in pyrolite melt with 5 wt% H_2O (Matsukage et al., 2005), enstatite melt with 4.5–10 wt% H_2O (Karki et al., 2020; Mookherjee et al., 2008), silica melt with 8.25 wt% H_2O (Bajgain et al., 2015; Karki & Stixrude, 2010), albite melt with 1.9–6.1 wt% H_2O (Ochs & Lange, 1997) and basalt melt with 5–8 wt% H_2O (Bajgain et al., 2015; Sakamaki et al., 2006). Thus, with increasing pressure the partial molar volume of H_2O becomes increasingly insensitive to both temperature and melt composition.

The partial molar volumes of H_2O reported for the komatiite-fayalite mixture at 1773 and 2073 K appear underestimated (Agee, 2008). It should be noted that the partial molar volume of 4 cm^3/mol at 7.9 GPa is considered a rough estimate, as the dry EOS was extrapolated from the data of two studies at 0–1.5 GPa (Agee, 2008; Lange & Carmichael, 1987). At 2 GPa, the partial molar volume should in principle be better constrained, and the reason for the discrepancy is unknown. It was proposed that the change in partial molar volume is very high between 0 and 2 GPa, resulting in little additional compression at higher pressures (Agee, 2008); however, it appears that the decrease in volume may not be as significant as previously suggested.

At approximately ambient pressure and 2000 K, the experimentally-determined partial molar volume of CO_2 in peridotite melt with 2.5 wt% CO_2 is 34.8(2.5) cm^3/mol (Sakamaki et al., 2011), which agrees excellently with our calculated value of 34.4 cm^3/mol at 2000 K. In komatiite melt with 5.7 wt% CO_2 at 2123 K, Duncan and Agee (2011) find partial molar volumes of 23.71(1.3) and 22.06(1.29) at 4.3 and 5.5 GPa, respectively, which are about 10% higher than our calculated values at 2000 K, and may be consistent with the temperature difference, within uncertainty. In basalt melt with 5 wt% CO_2 at 19–20 GPa and 2573 K, Ghosh et al. (2007) determine a CO_2 partial molar volume of 20.98 cm^3/mol, which is much larger than our calculated values of 13.7 cm^3/mol and 16 cm^3/mol at 2000 K and 3000 K, respectively. The reason for the discrepancy may be a result of the compositional and structural differences between the melts; however, it is not well understood and highlights the need for additional experiments at high pressures to more accurately constrain the compressibility behavior of CO_2.

Our calculated partial molar volumes for CO_2 in pyrolite melt are in excellent agreement with the results of the *ab initio* molecular dynamics simulations on enstatite melt with 5.2–10.9 wt% CO_2 (Ghosh et al., 2017; Karki et al., 2020). Furthermore, Karki et al. (2020) find that the sum of the partial molar volumes of H_2O and CO_2 overlap with the partial molar volume of H_2O and CO_2 in their mixed-volatile melt, implying that there is no interaction between the carbon and hydrogen in the melts, which is in agreement with our observations. Guillot and Sator (2011) used classical molecular dynamics to calculate the partial molar volume
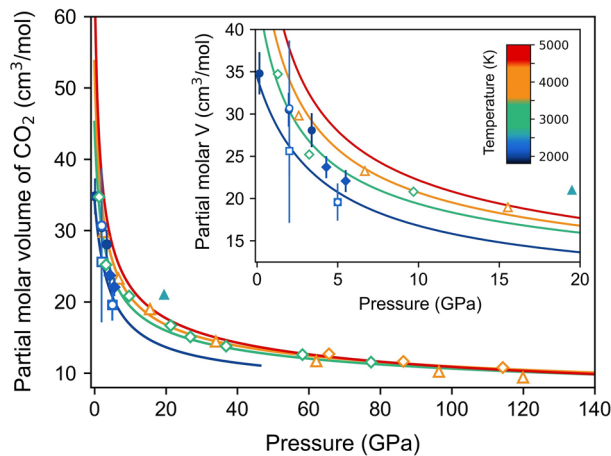
Figure 4. Partial molar volumes of CO_2 in magmatic melts with 2–11 wt% CO_2. See Figure S4 for melts with higher concentrations of CO_2. Curves are the results of our simulations of pyrolite + $4CO_2$ (5.2 wt% CO_2) at 2000 K (blue), 3000 K (green), 4000 K (orange) and 5000 K (red). Experimental data are shown as filled symbols: basalt melt with 5 wt% CO_2 at 2573 K (upward-pointing triangles; Ghosh et al., 2007), peridotite melt with 2.5 wt% CO_2 at 2000 K (circles; Sakamaki et al., 2011), and komatiite melt with 5.7 wt% CO_2 at 2123 K (diamonds; Duncan & Agee, 2011). Data from *ab initio* molecular dynamics simulations are shown as open symbols: enstatite melt with 10.9 wt% CO_2 at 3,000–4000 K (open diamonds; Karki et al., 2020) and enstatite melt with 5.2 wt% CO_2 at 4000 K (open upward-pointing triangles; Ghosh et al., 2017). Classical simulations at 2273 K by Guillot and Sator (2011) on kimberlite and MORB melts with 2–7 wt% CO_2 are shown as open squares and open circles, respectively. Inset shows a magnification of the 0–20 GPa region.

of CO_2 in kimberlite and MORB melts where the concentration of CO_2 in the melt was allowed to change with pressure based on its solubility behavior (Figure 4). The concentration of CO_2 in the melts increased from about 2–40 wt% CO_2 from 2 to 15 GPa. In the CO_2 concentration range of 2–7 wt% CO_2, the partial molar volumes of CO_2 in the MORB and kimberlite melts agree well with the results of our simulations. Due to the strong effect of CO_2 concentration on the partial molar volume of CO_2 above concentrations of roughly 10–15 wt% CO_2, we do not include melt compositions with high CO_2 concentrations in Figure 4 and instead report them in Figures S4 and S5.

Experiments on silicate glasses at ambient conditions suggest that the concentration of CO_2 and the chemistry of the melts affect the CO_2 partial molar volume (Seifert et al., 2013). The chemistry of the melts directly impacts the partial molar volume of CO_2 by dictating the speciation of carbon (i.e., the coordination of carbon by oxygen) in the melt. Furthermore, Seifert et al. (2013) find that the composition of the melt also influences the relationship between the partial molar volume CO_2 and the concentration of CO_2. The partial molar volume of CO_2 in basalt, phonolite, and rhyolite glasses with 1 mol% CO_2 is about 23, 27, and 30 cm³/mol, respectively. With increasing CO_2 concentration, the partial molar volume increases in the basalt glass and decreases in the rhyolite and phonolite glasses, such that by 100 mol% CO_2 (from a linear extrapolation), the volume of CO_2 is 26.6(1.8), 25.4(9), and 22.1(8) cm³/mol for the basalt, rhyolite, and phonolite glasses, respectively. Here we find that for ultramafic melts (i.e., enstatite and pyrolite compositions) at 4000 K, the addition of CO_2 decreases the partial molar volume of CO_2, at least in the CO_2 concentration range of 5–30 wt% CO_2 (Figure S4). The volume of pure CO_2, however, is larger than the partial molar volume of CO_2 within all of the melts up to about 60 GPa, at which point the data converges, within uncertainty. At ∼2000 K, the effect of CO_2 concentration on the CO_2 partial molar volume is less clear due to the scarcity of available data, the consequent scatter in the data and the vastly different compositions that we compare, which is also a consequence of the scarcity of data (Figure S5). We compare our results on pyrolite melt with 5.2 wt% CO_2 to the results of classical simulations on kimberlite and MORB melts with 2–40 wt% CO_2 at 2273 K Guillot and Sator (2011) and experiments on peridotite melt with 2.5 wt% CO_2 at 2000 K (Sakamaki et al., 2011), komatiite melt with 5.7 wt% CO_2 at 2123 K (Duncan & Agee, 2011), and $K_2Ca(CO_3)_2$ melt (37 wt% CO_2) at 1950 K (Dobson et al., 1996). Despite the different compositions, it appears that at 2000 K the addition of CO_2 generally increases the CO_2 partial molar volume within the concentration range of 2–40 wt% CO_2. Perhaps the most important conclusion from this analysis is that the effect of composition and CO_2 concentration on the partial molar volume of CO_2 is complex and additional studies are required to resolve these effects.

To our best knowledge, there are no experimental measurements at temperatures of 3000 K and above due to experimental limitations. Our theoretical results at upper-mantle and mid-mantle pressures show a clear increase of the partial molar volumes for both H_2O and CO_2 with increasing temperature. The temperature dependence generally decreases with pressure, such that at 100 GPa the partial molar volumes of H_2O and CO_2 are 6.2 and 10.6 cm³/mol, respectively, independent of temperature. The partial molar volume of CO_2 is thus only 1.7 times larger than H_2O at high pressure. Although there are differences in the absolute densities between our simulations on pyrolite melt and experiments on peridotite melts (Figure S3), which are nearly identical in composition, and between computational studies on ultramafic melts due to the use of different computational methods (i.e., classical interatomic potentials compared to density functional theory, local density approximation compared to the general gradient approximation, and choice in pseudopotentials), the partial molar volumes of H_2O and CO_2 appear to be nearly insensitive to these differences. In particular, it is known that the local density approximation and the general gradient approximation respectively overestimate and underestimate the cohesive energies, resulting in an overestimation and un-

derestimation of absolute densities, yet there is an excellent agreement for the partial molar volumes of CO_2 and H_2O in ultramafic melts using the local gradient approximation (Ghosh et al., 2017; Mookherjee et al., 2008) and the generalized gradient approximation (Karki et al., 2020; this study). Thus, the partial molar volume of H_2O and CO_2 provide a useful tool for benchmarking and discerning subtle differences between volatile-bearing melts when other properties may differ due to differences in methodology. The partial molar volumes of H_2O and CO_2 in pyrolite melt as a function of pressure and temperature are available at https://doi.org/10.5281/zenodo.4334000.

3.3. Structure of the Melts

The bond distances are relatively rigid in the pressure range of the Earth's mantle. The compression, even at pressures corresponding to the base of the magma ocean, is not enough to reduce the bonds by more than 10%, and in fact, bond lengths for Si-O even increase with increasing pressure up to mid-mantle pressures. Consequently, the compression is accommodated in the melts by more efficient packing, which is reflected in the increase of the coordination number. In a detailed analysis of the structure of dry, non-carbonated, pyrolytic melts (Solomatova & Caracas, 2019) we have seen that all the coordination polyhedra of the cations by anions increase consistently with compression. At ambient pressure, the melts are dominated by long-living SiO_4 (and AlO_4) tetrahedra, with minor 3-fold and 5-fold coordination polyhedra. As the pressure increases, the melts start to be dominated by SiO_5 pentahedra at mid-mantle conditions, with more and more SiO_6 and fewer SiO_4 components. At the base of the magma ocean the melts would be dominated by distorted SiO_6 octahedra, with a strong SiO_5 and SiO_7 component (Figure 5). At 0 GPa, the silica polyhedra exist as a mixture of isolated and corner-sharing tetrahedra. With increasing pressure, as the polyhedra grow in coordination number, they become increasingly corner- and edge-sharing.

Hydrogen exists as hydroxides in the pyrolite melt at all temperatures examined in this study, independent of the way hydrogen was inserted into the melt. Bridging O-H-O configurations are approached at high pressure, but symmetrization is never achieved, and hydrogen seems to preferentially remain bonded to one oxygen atom. Experiments have shown that the proportion of $OH/(OH + H_2O)$ in silicate glasses decreases with the total water content (Stolper, 1982) and strongly increases with increasing temperature (Behrens, 2020; Shen & Keppler, 1995; Zhang, 1999). For example, the proportion of $OH/(OH + H_2O)$ in haplogranitic and sodium alumino-silicate glasses increases from about 25%–35% at ∼300 K to 65%–75% at ∼1200 K (Nowak & Behrens, 2001; Shen & Keppler, 1995). Although there are no experimental data on hydrogen speciation in silicate glasses at ≥2000 K, we can extrapolate from these results that hydrogen would exist predominantly in the form of OH in silicate melts with H_2O concentrations corresponding to our study (i.e., 1–5 wt% H_2O), in agreement with our findings.

In contrast, the coordination of carbon by oxygen increases with increasing pressure, such that it exists predominantly as CO_2 at ambient pressure, CO_3 at mid-mantle pressures and CO_4 at lowermost mantle pressures (Figure 5; see also Solomatova et al., 2019). The presence of carbon in either form does not affect the coordination trend of silicon. Even more interestingly, carbon tends to replace oxygen in the melt and to polymerize, forming together with silicon and iron large chemical complexes, particularly in the more reduced melts (Belonoshko et al., 2016; Karki et al., 2020; Solomatova et al., 2019). The formation of such complexes likely affects the relative density and compressibility of the carbonated melts, as shown by the systematically larger bulk moduli relative to pure pyrolite at 135 GPa where the addition of hydrous volatiles has the opposite effect (Table 2). These complexes could have been leached down and sequestered into the core during core formation (Belonoshko et al., 2016; Solomatova et al., 2019; Solomatova et al., 2020).

The degree of polymerization can be described by the average coordination number of oxygen by silicon, 2 being representative of a fully polymerized melt (e.g., SiO_2) and 1 being representative of a depolymerized melt (e.g., Mg_2SiO_4). It has been previously shown that the addition of water decreases the polymerization of SiO_2 and $MgSiO_3$ melts, possibly due to the addition of hydrogen itself (Karki et al., 2010; Mookherjee et al., 2008). Here, we attribute the dominant change in structure of the melt to the addition of oxygen in the form of H_2O or other volatiles, such as CO or CO_2. Figure 6 shows the increase of the polymerization in the melt as reflected in the increase of coordination number of oxygen by silicon as a function of pressure. Close to ambient pressure, the coordination number is around 1, roughly corresponding to isolated
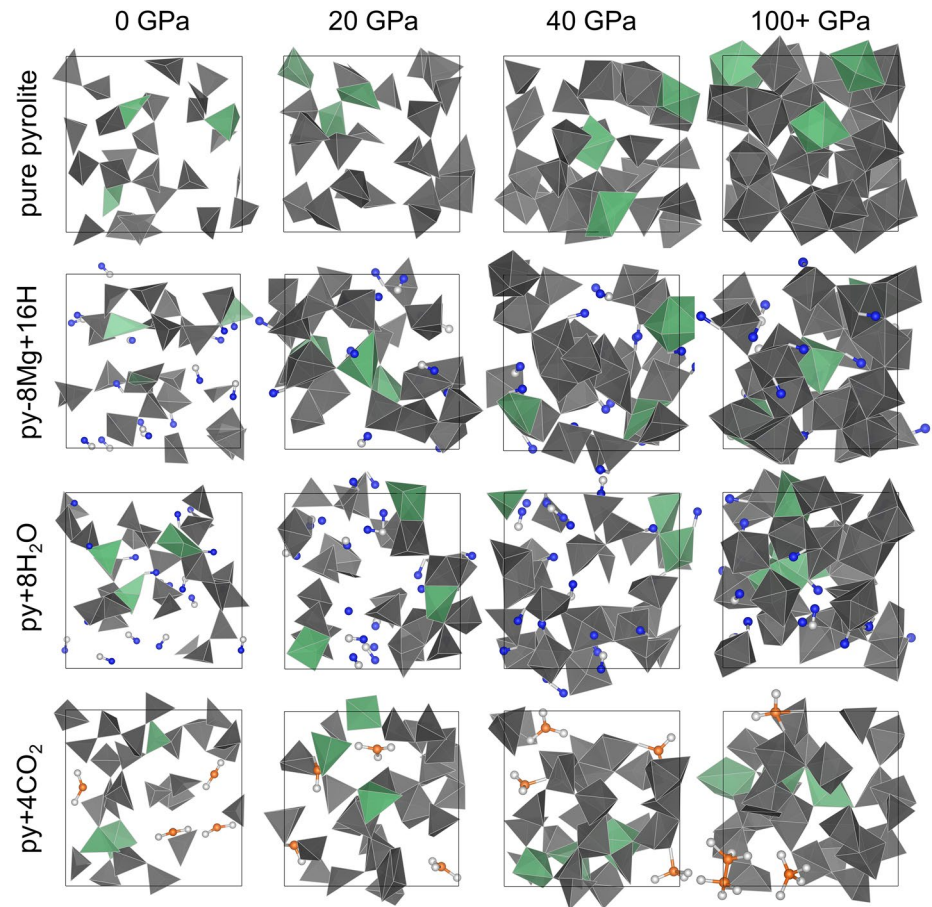
Figure 5. The evolution of the silica-alumina network in volatile-free and volatile-bearing pyrolite melts as a function of pressure at 4000 K. Mg, Fe, Ca, and Na polyhedra are omitted to show the silica-alumina polymerization network. Only the silica polyhedra (gray), alumina polyhedra (green), hydrogen atoms (blue), carbon atoms (orange), and (C,H)-bonded oxygen atoms (white) are shown. Simulations are conducted at constant density. The exact pressure of each simulation is 0, 15, 48, and 148 GPa for pure pyrolite (first row); 0, 24, 43 and, 132 GPa for py-8Mg+16H (second row); 0, 22, 38, and 113 GPa for py+8H$_2$O (third row); and 0, 20, 36, and 108 GPa for py+4CO$_2$ (fourth row). It should be noted that each cell is an example of only one step out of tens of thousands of time steps from the simulations.

polyhedra. Pure pyrolite melt has the largest coordination of oxygen by silicon at around 1.1, and this value generally decreases with an increasing amount of volatiles, decreasing to 0.85 for the most carbonated melt, py+8CO$_2$ (2.68% C). Under compression, the coordination number increases and begins to saturate above megabar pressures. The maximum coordination number is again highly dependent on composition and amount of volatiles added. At 140 GPa, the smallest coordination number of oxygen by silicon is 1.4 for py+8CO$_2$ (2.68% C), while the highest is 1.6 for the systems with hydrogen added through magnesium substitution (Figure 6).

The coordination number of oxygen by silicon decreases linearly with an increasing amount of oxygen added to the system, at all pressures (Figure 7). At 0 GPa, the addition of hydrogen in the form of H substitution for Mg results in a slight decrease in the coordination number of oxygen by silicon, but the effect is secondary to the effect of adding hydrogen in the form of H$_2$O, and in fact, with pressure, the addition of hydrogen in the form of H slightly increases the coordination number of oxygen by silicon. We acknowledge, that the addition of carbon may also slightly depolymerize the melt further, as seen by the slightly higher coordination number of oxygen by silicon in pyrolite with 4CO$_2$ compared to pyrolite with 8CO, but the effect is secondary.
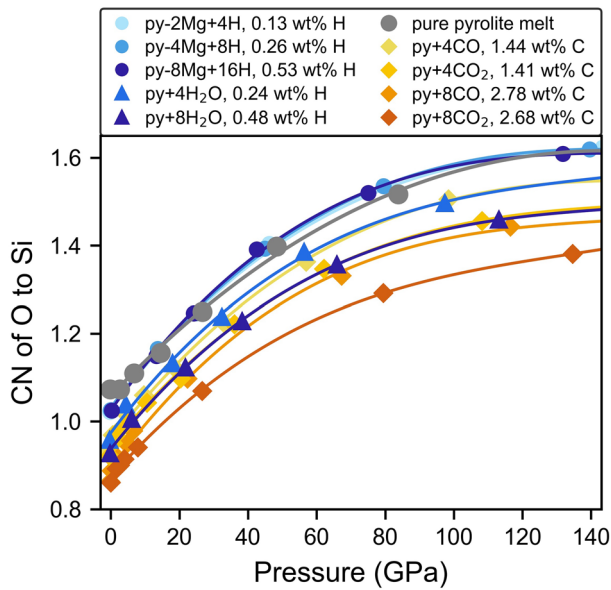
Figure 6. Average coordination number (CN) of oxygen to silicon at 4000 K as a function of pressure. Third-order polynomial fits were used to compare coordination values at equivalent pressures in Figure 7. The coordination number of oxygen to silicon describes the degree of polymerization of the melt where 1 represents a depolymerized melt and 2 represents a fully-polymerized melt. The addition of oxygen from the volatile molecules decreases the polymerization of the melt.

The addition of the equivalent amount of oxygen in the form of different types of volatiles (e.g., 4CO and $4H_2O$ molecules) has nearly the same effect on the coordination number of oxygen by silicon. The addition of volatiles to a silicate melt results in a depolymerization reaction involving SiO_4^{4-} monomers and three forms of oxygen: singly bonded non-bridging O^- (NBO), doubly bonded bridging O^0 (BO) and free oxygen O^{2-} (Belmonte et al., 2017; Ottonello et al., 2001; Ottonello & Moretti, 2004). The interaction of the added volatile with the silicate melt can be described by the dissociation of the volatile (e.g., $CO_2 \Leftrightarrow C^{4+} + 2O^{2-}$) followed by an anionic interaction (i.e., $O^0 + O^{2-} \Leftrightarrow 2O^-$; Toop & Samis, 1962). The creation of non-bridging oxygens (O^-) from bridging (O^0) and free (O^{2-}) oxygen effectively decreases the coordination of oxygen by silicon and hence, the degree polymerization of the silicate melt. Thus, the oxidation state of the melts dictates the degree of polymerization and consequently, the viscosity of the melts. Although, the addition of different types of volatiles with an equivalent amount of oxygen does not affect melt viscosity, the type of volatile added does play a role in the relative buoyancy of the melts (Figure 2).

4. Conclusions and Implications

We find that at uppermost-mantle pressures, the compressibility and density of the pyrolite melts are strongly affected by the addition of volatile species, whereas at lowermost-mantle pressures, the effect of volatile species on density and compressibility is much weaker. While at low pressure, the addition of any volatiles increases the melt's compressibility, at high pressures, only the hydrous melts increase its compressibility, while the carbonated melts are systematically slightly more incompressible, likely due to the mechanism of carbon incorporation into the melt. Furthermore, we find that the polymerization of the melt is strongly affected by the amount of oxygen added to the system in the form 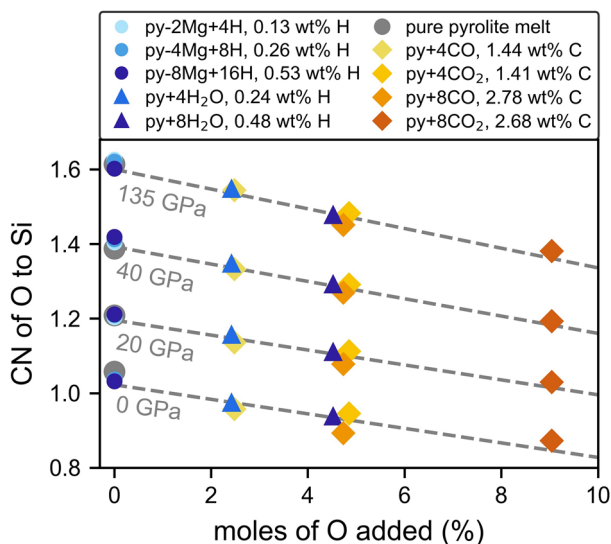of volatiles and only very weakly affected by the type of volatiles (H_2O vs. CO_2). At 0 GPa and 3000 K, the addition of 2.2 wt% H_2O and 5.2 wt% CO_2 decreases the melt's density by 6.6% and 6.1%, respectively. At core-mantle boundary conditions (135 GPa and 4000 K) the effect is much smaller, where the addition of 2.2 and 4.3 wt% of H_2O decreases the density by about 1.5% and 2.9%, respectively, and the addition of 5.2 and 9.8 wt% CO_2 decreases the density by about 1.1% and 1.7%, respectively.

We compute the partial molar volumes for H_2O and CO_2 and find an excellent agreement with experiments at ~2000 K. Our results also help understand some experimental discrepancies at low pressures and temperatures. We find that the partial molar volumes depend on temperature at low pressures, but with compression the dependence vanishes, and the partial molar volumes converge to 6.2 cm^3/mol for H_2O and at 10.6 cm^3/mol for CO_2 at 100 GPa. The partial molar volume of CO_2 is 1.7 times larger than H_2O at high pressures. Thus, the specific type of volatile species inserted into the melt affects the density of the melt, but only weakly affects the coordination of oxygen by silicon, which is much more strongly affected by the total amount of oxygen added to the system.

Figure 7. Average coordination number (CN) of oxygen by silicon at 4000 K as a function of the mole percent of oxygen added. The coordination decreases linearly as more oxygen is added to the system with only a weak sensitivity to the type of volatile added.

Our numerical results show that the presence of volatiles would affect only weakly the pressure of the density crossover between crystals and pyrolite melts in the magma ocean. As the absolute effect of volatiles on the density of pyrolite melts at magma ocean conditions is on the order

of 0.1 g/cm^3, compared to results in Caracas et al. (2019), this would move the density crossover pressure by tens of GPa. The presence of volatiles would increase the volume of the basal magma ocean. However, the effect of volatiles is more important on the global circulation of magma in a convecting magma ocean, as the volatiles increase the buoyancy of the ascending circulation. As the upward flow approaches the surface, the density difference between volatile-rich and volatile-poor magmas increases and the flow is accelerated. At the contact with the atmosphere, much of the volatiles would be lost. The magmas in the downward flow, colder and depleted in volatiles, would become even more negatively buoyant. Consequently, the circulation of the magma ocean would be accelerated along the two branches of the convection cells. This in turn would increase the rate at which magma comes in contact with the surface, promoting more vigorous degassing, more rapid changes of the atmospheric chemistry and a more pronounced participation of the deep Earth, overall enhancing the chemical interactions between the early atmosphere and magma ocean.

Data Availability Statement

As part of the FAIR data policy, all pressure-volume-density data are available at https://doi.org/10.5281/zenodo.4333936 and the partial molar volumes of H_2O and CO_2 are available at https://doi.org/10.5281/zenodo.4334000.

References

Agee, C. B. (1998). Crystal-liquid density inversions in terrestrial and lunar magmas. *Physics of the Earth and Planetary Interiors*, *107*(1–3), 63–74. https://doi.org/10.1016/S0031-9201(97)00124-6

Agee, C. B. (2008). Static compression of hydrous silicate melt and the effect of water on planetary differentiation. *Earth and Planetary Science Letters*, *265*(3–4), 641–654. https://doi.org/10.1016/j.epsl.2007.11.010

Agee, C. B., & Walker, D. (1988). Static compression and olivine flotation in ultrabasic silicate liquid. *Journal of Geophysical Research*, *93*(B4), 3437–3449. https://doi.org/10.1029/JB093iB04p03437

Agee, C. B., & Walker, D. (1993). Olivine flotation in mantle melt. *Earth and Planetary Science Letters*, *114*(2–3), 315–324. https://doi.org/10.1016/0012-821X(93)90033-6

Andrault, D., Petitgirard, S., Lo Nigro, G., Devidal, J. L., Veronesi, G., Garbarino, G., & Mezouar, M. (2012). Solid–liquid iron partitioning in Earth's deep mantle. *Nature*, *487*, 354–357. https://doi.org/10.1038/nature11294

Bajgain, S., Ghosh, D. B., & Karki, B. B. (2015). Structure and density of basaltic melts at mantle conditions from first-principles simulations. *Nature Communications*, *6*(1), 1–7. http://doi.org/10.1038/ncomms9578

Ballmer, M. D., Houser, C., Hernlund, J. W., Wentzcovitch, R. M., & Hirose, K. (2017). Persistence of strong silica-enriched domains in the Earth's lower mantle. *Nature Geoscience*, *10*(3), 236–240. http://doi.org/10.1038/ngeo2898

Ballmer, M. D., Lourenço, D. L., Hirose, K., Caracas, R., & Nomura, R. (2017). Reconciling magma-ocean crystallization models with the present-day structure of the Earth's mantle. *Geochemistry, Geophysics, Geosystems*, *18*, 2785–2806. https://doi.org/10.1002/2017GC006917

Behrens, H. (2020). Water speciation in oxide glasses and melts. *Chemical Geology*, *558*, 119850. https://doi.org/10.1016/j.chemgeo.2020.119850

Belmonte, D., Ottonello, G., Zuccolini, M. V., & Attene, M. (2017). The system MgO-Al_2O_3-SiO_2 under pressure: A computational study of melting relations and phase diagrams. *Chemical Geology*, *461*, 54–64. https://doi.org/10.1016/j.chemgeo.2016.11.011

Belonoshko, A. B., Lukinov, T., Rosengren, A., Bryk, T., & Litasov, K. D. (2016). Synthesis of heavy hydrocarbons at the core-mantle boundary. *Scientific Reports*, *5*, 18382. https://doi.org/10.1038/srep18382

Canup, R. M. (2012). Forming a moon with an Earth-like composition via a giant impact. *Science*, *338*(6110), 1052–1055. http://doi.org/10.1126/science.1226073

Caracas, R., Hirose, K., Nomura, R., & Ballmer, M. D. (2019). Melt–crystal density crossover in a deep magma ocean. *Earth and Planetary Science Letters*, *516*, 202–211. http://doi.org/10.1016/j.epsl.2019.03.031

Cody, G. D., Heying, E., Alexander, C. M. O., Nittler, L. R., Kilcoyne, A. L. D., Sandford, S. A., & Stroud, R. M. (2011). Establishing a molecular relationship between chondritic and cometary organic solids. *Proceedings of the National Academy of Sciences*, *108*(48), 19171–19176. http://doi.org/10.1073/pnas.1015913108

Ćuk, M., & Stewart, S. S. (2012). Making the Moon from a fast-spinning Earth: A giant impact followed by resonant despinning. *Science*, *338*(6110), 1047–1052. http://doi.org/10.1126/science.1225542

de Koker, N., Karki, B. B., & Stixrude, L. (2013). Thermodynamics of the MgO–SiO_2 liquid system in Earth's lowermost mantle from first principles. *Earth and Planetary Science Letters*, *361*(c), 58–63. http://doi.org/10.1016/j.epsl.2012.11.026

Dobson, D. P., Jones, A. P., Rabe, R., Sekine, T., Kurita, K., Taniguchi, T., & Urakawa, S. (1996). In-situ measurement of viscosity and density of carbonate melts at high pressure. *Earth and Planetary Science Letters*, *143*(1–4), 207–215. https://doi.org/10.1016/0012-821X(96)00139-2

Duncan, M. S., & Agee, C. B. (2011). The partial molar volume of carbon dioxide in peridotite partial melt at high pressure. *Earth and Planetary Science Letters*, *312*(3–4), 429–436. https://doi.org/10.1016/j.epsl.2011.10.021

Dziewonski, A. M., & Anderson, D. L. (1981). Preliminary reference earth model. *Physics of the Earth and Planetary Interiors*, *25*(4), 297–356.

Elkins-Tanton, L. T. (2008). Linked magma ocean solidification and atmospheric growth for Earth and Mars. *Earth and Planetary Science Letters*, *271*(1–4), 181–191. https://doi.org/10.1016/j.epsl.2008.03.062

Fiquet, G., Auzende, A. L., Siebert, J., Corgne, A., Bureau, H., Ozawa, H., & Garbarino, G. (2010). Melting of Peridotite to 140 Gigapascal. *Science*, *329*(5998), 1516–1518. http://doi.org/10.1126/science.1192448

Ghosh, D. B., Bajgain, S. K., Mookherjee, M., & Karki, B. B. (2017). Carbon-bearing silicate melt at deep mantle conditions. *Scientific reports*, *7*(1), 1–8. https://doi.org/10.1038/s41598-017-00918-x

Ghosh, S., Ohtani, E., Litasov, K., Suzuki, A., & Sakamaki, T. (2007). Stability of carbonated magmas at the base of the Earth's upper mantle. *Geophysical Research Letters*, *34*(22), L22312. https://doi.org/10.1029/2007GL031349

Guillot, B., & Sator, N. (2011). Carbon dioxide in silicate melts: A molecular dynamics simulation study. *Geochimica et Cosmochimica Acta*, *75*(7), 1829–1857. https://doi.org/10.1016/j.gca.2011.01.004

Harvey, J.-P., & Asimow, P. D. (2015). Current limitations of molecular dynamics simulations as probes of thermo-physical behavior of silicate melts. *American Mineralogist*, *100*(8–9), 1866–1882. http://doi.org/10.2138/am-2015-5159

Karki, B. B., Bhattarai, D., Mookherjee, M., & Stixrude, L. (2010). Visualization-based analysis of structural and dynamical properties of simulated hydrous silicate melt. *Physics and Chemistry of Minerals*, *37*(2), 103–117. https://doi.org/10.1007/s00269-009-0315-1

Karki, B. B., Ghosh, D. B., & Banjara, D. (2020). Mixed incorporation of carbon and hydrogen in silicate melts under varying pressure and redox conditions. *Earth and Planetary Science Letters*, *549*, 116520. https://doi.org/10.1016/j.epsl.2020.116520

Karki, B. B., Ghosh, D. B., Maharjan, C., Karato, S. I., & Park, J. (2018). Density-pressure profiles of Fe-bearing $MgSiO_3$ liquid: Effects of valence and spin states, and implications for the chemical evolution of the lower mantle. *Geophysical Research Letters*, *45*(9), 3959–3966. https://doi.org/10.1029/2018GL077149

Kono, Y., Shibazaki, Y., Kenney-Benson, C., Wang, Y., & Shen, G. (2018). Pressure-induced structural change in $MgSiO_3$ glass at pressures near the Earth's core–mantle boundary. *Proceedings of the National Academy of Sciences*, *115*(8), 1742–1747. http://doi.org/10.1073/pnas.1716748115

Kresse, G., & Furthmüller, J. (1996). Efficiency of ab-initio total energy calculations for metals and semiconductors using a plane-wave basis set. *Computational Materials Science*, *6*(1), 15–50. https://doi.org/10.1016/0927-0256(96)00008-0

Kresse, G., & Hafner, J. (1993). Ab initio molecular dynamics for liquid metals. *Physical Review Journal*, *B47*, 558. https://doi.org/10.1103/PhysRevB.47.558

Labrosse, S., Hernlund, J. W., & Coltice, N. (2007). A crystallizing dense magma ocean at the base of the Earth's mantle. *Nature*, *450*(7171), 866–869. http://doi.org/10.1038/nature06355

Lange, R. A., & Carmichael, I. S. (1987). Densities of Na_2O-K_2O-CaO-MgO-FeO-Fe_2O_3-Al_2O_3-TiO_2-SiO_2 liquids: New measurements and derived partial molar properties. *Geochimica et Cosmochimica Acta*, *51*(11), 2931–2946. https://doi.org/10.1016/0016-7037(87)90368-1

Lock, S. J., Stewart, S. T., Petaev, M. I., Leinhardt, Z., Mace, M. T., Jacobsen, S. B., & Ćuk, M. (2018). The Origin of the Moon Within a Terrestrial Synestia. *Journal of Geophysical Research: Planets*, *123*(4), 910–951. http://doi.org/10.1002/2017JE005333

Matsukage, K. N., Jing, Z., & Karato, S. I. (2005). Density of hydrous silicate melt at the conditions of Earth's deep upper mantle. *Nature*, *438*(7067), 488–491. https://doi.org/10.1038/nature04241

McDonough, W. F., & Sun, S. S. (1995). The composition of the Earth. *Chemical Geology*, *120*, 223–253. http://doi.org/10.1016/0009-2541(94)00140-4

Mookherjee, M., Stixrude, L., & Karki, B. (2008). Hydrous silicate melt at high pressure. *Nature*, *452*(7190), 983–986. https://doi.org/10.1038/nature06918

Murakami, M., & Bass, J. D. (2010). Spectroscopic evidence for ultrahigh-pressure polymorphism in SiO_2 glass. *Physical Review Letters*, *104*(2), 025504. http://doi.org/10.1103/PhysRevLett.104.025504

Nomura, R., Ozawa, H., Tateno, S., Hirose, K., Hernlund, J., Muto, S., et al. (2011). Spin crossover and iron-rich silicate melt in the Earth's deep mantle. *Nature*, *473*(7346), 199–202. http://doi.org/10.1038/nature09940

Nowak, M., & Behrens, H. (2001). Water in rhyolitic magmas: Getting a grip on a slippery problem. *Earth and Planetary Science Letters*, *184*(2), 515–522. https://doi.org/10.1016/S0012-821X(00)00343-5

Ochs, F. A., III, & Lange, R. A. (1997). The partial molar volume, thermal expansivity, and compressibility of H_2O in $NaAlSi_3O_8$ liquid: new measurements and an internally consistent model. *Contributions to Mineralogy and Petrology*, *129*(2–3), 155–165. https://doi.org/10.1007/s004100050329

Ottonello, G., & Moretti, R. (2004). Lux-Flood basicity of binary silicate melts. *Journal of Physics and Chemistry of Solids*, *65*(8–9), 1609–1614. https://doi.org/10.1016/j.jpcs.2004.01.012

Ottonello, G., Moretti, R., Marini, L., & Zuccolini, M. V. (2001). Oxidation state of iron in silicate glasses and melts: A thermochemical model. *Chemical Geology*, *174*(1–3), 157–179. https://doi.org/10.1016/S0009-2541(00)00314-4

Park, S. Y., & Lee, S. K. (2018). Probing the structure of Fe-free model basaltic glasses: A view from a solid-state ^{27}Al and ^{17}O NMR study of Na-Mg silicate glasses, Na_2O-MgO-Al_2O_3-SiO_2 glasses, and synthetic Fe-free KLB-1 basaltic glasses. *Geochimica et Cosmochimica Acta*, *238*, 563–579. https://doi.org/10.1016/j.gca.2018.07.032

Perdew, J. P., Burke, K., & Ernzerhof, M. (1996). Generalized gradient approximation made simple. *Physical Review Letters*, *77*, 3865. https://doi.org/10.1103/PhysRevLett.77.3865

Petitgirard, S. (2017). Density and structural changes of silicate glasses under high pressure. *High Pressure Research*, *37*(2), 200–213. http://doi.org/10.1080/08957959.2017.1302444

Prescher, C., Prakapenka, V. B., Stefanski, J., Jahn, S., Skinner, L. B., & Wang, Y. (2017). Beyond sixfold coordinated Si in SiO_2 glass at ultrahigh pressures. *Proceedings of the National Academy of Sciences*, *114*(38), 10041–10046. http://doi.org/10.1073/pnas.1708882114

Rigden, S. M., Ahrens, T. J., & Stolper, E. M. (1984). Densities of liquid silicates at high pressures. *Science*, *226*(4678), 1071–1074. https://doi.org/10.1126/science.226.4678.1071

Sahle, C. J., Sternemann, C., Schmidt, C., Lehtola, S., Jahn, S., Simonelli, L., et al. (2013). Microscopic structure of water at elevated pressures and temperatures. *Proceedings of the National Academy of Sciences*, *110*(16), 6301–6306. http://doi.org/10.1073/pnas.1220301110

Sakamaki, T., Ohtani, E., Urakawa, S., Suzuki, A., & Katayama, Y. (2009). Measurement of hydrous peridotite magma density at high pressure using the X-ray absorption method. *Earth and Planetary Science Letters*, *287*(3–4), 293–297. http://doi.org/10.1016/j.epsl.2009.07.030

Sakamaki, T., Ohtani, E., Urakawa, S., Suzuki, A., & Katayama, Y. (2010). Density of dry peridotite magma at high pressure using an X-ray absorption method. *American Mineralogist*, *95*(1), 144–147. http://doi.org/10.2138/am.2010.3143

Sakamaki, T., Ohtani, E., Urakawa, S., Terasaki, H., & Katayama, Y. (2011). Density of carbonated peridotite magma at high pressure using an X-ray absorption method. *American Mineralogist*, *96*(4), 553–557. http://doi.org/10.2138/am.2011.3577

Sakamaki, T., Suzuki, A., & Ohtani, E. (2006). Stability of hydrous melt at the base of the Earth's upper mantle. *Nature*, *439*(7073), 192–194. https://doi.org/10.1038/nature04352

Sanloup, C. (2016). Density of magmas at depth. *Chemical Geology*, *429*(C), 51–59. http://doi.org/10.1016/j.chemgeo.2016.03.002

Sanloup, C., Drewitt, J. W. E., Konôpková, Z., Dalladay-Simpson, P., Morton, D. M., Rai, N., et al. (2013). Structural change in molten basalt at deep mantle conditions. *Nature*, *1–6*, 104–107. http://doi.org/10.1038/nature12668

Seifert, R., Malfait, W. J., Lerch, P., & Sanchez-Valle, C. (2013). Partial molar volume and compressibility of dissolved CO_2 in glasses with magmatic compositions. *Chemical Geology*, *358*, 119–130. https://doi.org/10.1016/j.chemgeo.2013.09.007

Shen, A., & Keppler, H. (1995). Infrared spectroscopy of hydrous silicate melts to 1000 C and 10 kbar: Direct observation of H_2O speciation in a diamond-anvil cell. *American Mineralogist*, *80*(11–12), 1335–1338. https://doi.org/10.2138/am-1995-11-1223

Solomatova, N. V., & Caracas, R. (2019). Pressure-induced coordination changes in a pyrolytic silicate melt from ab initio molecular dynamics simulations. *Journal of Geophysical Research: Solid Earth*, *124*(11), 11232–11250. http://doi.org/10.1029/2019JB018238

Solomatova, N., Caracas, R., & Cohen, R. (2020). Carbon speciation and solubility in silicate melts. *Carbon in Earth's Interior*, *10*(1), 179–194. https://doi.org/10.1002/9781119508229.ch16

Solomatova, N. V., Caracas, R., & Manning, C. E. (2019). Carbon sequestration during core formation implied by complex carbon polymerization. *Nature Communications*, *10*(1), 1–7. http://doi.org/10.1038/s41467-019-08742-9

Spiekermann, G., Wilke, M., & Jahn, S. (2016). Structural and dynamical properties of supercritical H_2O–SiO_2 fluids studied by ab initio molecular dynamics. *Chemical Geology*, *426*(C), 85–94. http://doi.org/10.1016/j.chemgeo.2016.01.010

Stixrude, L., de Koker, N., Sun, N., Mookherjee, M., & Karki, B. B. (2009). Thermodynamics of silicate liquids in the deep Earth. *Earth and Planetary Science Letters*, *278*(3–4), 226–232. http://doi.org/10.1016/j.epsl.2008.12.006

Stolper, E. (1982). The speciation of water in silicate melts. *Geochimica et Cosmochimica Acta*, *46*(12), 2609–2620. https://doi.org/10.1016/0016-7037(82)90381-7

Suzuki, A., & Ohtani, E. (2003). Density of peridotite melts at high pressure. *Physics and Chemistry of Minerals*, *30*(8), 449–456. https://doi.org/10.1007/s00269-003-0322-6

Thomas, C. W., Liu, Q., Agee, C. B., Asimow, P. D., & Lange, R. A. (2012). Multi-technique equation of state for Fe_2SiO_4 melt and the density of Fe-bearing silicate melts from 0 to 161 GPa. *Journal of Geophysical Research*, *117*(B10), 144. http://doi.org/10.1029/2012JB009403

Toop, G., & Samis, C. S. (1962). Activities of ions in silicate melts. *Transactions of the Metallurgical Society of AIME*, *224*(5), 878.

Tronnes, R. G., Baron, M. A., Eigenmann, K. R., Guren, M. G., Heyn, B. H., Løken, A., & Mohn, C. E. (2019). Core formation, mantle differentiation and core-mantle interaction within Earth and the terrestrial planets. *Tectonophysics*, *760*, 165–198. http://doi.org/10.1016/j.tecto.2018.10.021

Wu, M., Liang, Y., Jiang, J.-Z., & Tse, J. S. (2012). Structure and properties of dense silica glass. *Nature Publishing Group*, *2*(1), 29–37. http://doi.org/10.1038/srep00398

Xu, M., Jing, Z., Van Orman, J. A., Yu, T., & Wang, Y. (2020). Density of $NaAlSi_2O_6$ melt at high pressure and temperature measured by In-Situ X-ray microtomography. *Minerals*, *10*(2), 161–215. http://doi.org/10.3390/min10020161

Zhang, Y. (1999). H_2O in rhyolitic glasses and melts: Measurement, speciation, solubility, and diffusion. *Reviews of Geophysics*, *37*(4), 493–516. https://doi.org/10.1029/1999RG9000.12